Materials Today 88 (2025) 12–23

Contents lists available at ScienceDirect

Materials Today

journal homepage: www.elsevier.com/locate/mattod

Short Communication

High entropy oxide epitaxial films with interface perpendicular magnetic anisotropy and tunnel magnetoresistance effect toward spintronic applications

Rombang Rizky Sihombing [a,b], Thomas Scheike [a], Jun Uzuhashi [a], Hideyuki Yasufuku [a], Tadakatsu Ohkubo [a], Zhenchao Wen [a], Seiji Mitani [a,b], Hiroaki Sukegawa [a,*]

[a] National Institute for Materials Science (NIMS), 1-2-1 Sengen, Tsukuba 305-0047, Japan
[b] Graduate School of Science and Technology, University of Tsukuba, Tsukuba 305-8577, Japan

ARTICLE INFO

Keywords:
High entropy oxides
Epitaxial growth
Spintronics
Perpendicular magnetization
Tunnel magnetoresistance

ABSTRACT

High entropy materials, usually composed of five or more constituent elements with a high mixing entropy have attracted increasing attention due to the marked development of new phases of multicomponent structural and functional materials. In particular, high entropy oxides (HEOs) are expected to realize their potential for electronic functionalities in spintronics, since the oxygen lattice required for achieving the functionalities remains besides the cation site disorder. In this study, we explored the HEO thin films with a rock-salt-like structure of LiTiMgAlGaO (L5O) for perpendicular magnetic anisotropy (PMA), which is induced at an interface with the CoFeB ferromagnet. The atomically homogeneous cation distributions in the 10–20 nm thick L5O films were achieved by atomic sputtering lamination on a MgO(001) single crystal substrate. The films were grown with a highly (001)-oriented epitaxial growth and have an atomically flat surface with an average roughness of 0.07 nm. We observed perpendicular magnetization of CoFeB on the L5O layer after 250–350 °C post-annealing, revealing that introduction of significantly large PMA at HEO/ferromagnet interfaces. A large interface PMA energy of up to ~ 0.8 erg/cm^2 at the interface was observed due to the achievement of structurally stable epitaxial layers with high crystallinity and sharp interfacial flatness of L5O and CoFeB interfaces. We also demonstrated that a tunnel magnetoresistance (TMR) ratio of up to 84 % at room temperature in epitaxial Fe/L5O/Fe(001) magnetic tunnel junctions (MTJs) with ultrathin MgO insertions at the L5O interfaces, indicating that the spin-dependent coherent tunneling mechanism is also observed in HEO-based MTJs. In addition, the L5O barrier exhibits low barrier heights less than 1 eV due to the bandgap reduction caused by the five cations. Our results of the high interface PMA energy, the relatively large TMR ratio, and the low barrier height show that the HEO materials can be a promising material family of ultra-thin barriers of MTJs for the next generation of spintronic devices such as ultra-high-density memory and spin artificial intelligence devices.

Introduction

High entropy materials gained prominence in the early 2000s, focusing primarily on metallic alloys with five or six major constituents [1,2]. Over time, "high entropy" has expanded to include other materials such as oxides, carbides, and borides. High entropy oxides (HEOs), as a subclass of high entropy materials, are materials stabilized by high configurational entropy, incorporating multiple metal cations in nearly equal atomic concentrations [3–6]. HEOs leverage chemical disorders to create novel solid solutions with unique local crystal structures that are rare in conventional materials. This disorder can affect physical properties such as electrochemical, magnetic, thermal, dielectric, and optical behavior, providing a means to tune these properties.

HEO ultra-thin films will represent a transformative leap forward in magnetic tunnel junctions (MTJs) beyond the conventional scope of materials development. The MTJ is the core structure in spintronic devices such as hard disk drives (HDDs) and magnetoresistive random access memories (MRAMs), consisting of a ferromagnetic layer (FM)/a few nm or less ultra-thin barrier/FM structure [7]. Ultra-thin HEOs with rock-salt or spinel structures in a (001) orientation can be a promising

---

* Corresponding author.
E-mail address: sukegawa.hiroaki@nims.go.jp (H. Sukegawa).

https://doi.org/10.1016/j.mattod.2025.06.025
Received 20 January 2025; Received in revised form 4 May 2025; Accepted 15 June 2025

barrier concept for a structurally stable MTJ barrier, which will lead to MTJs with a low resistance area product (*RA*) and a high interface perpendicular magnetic anisotropy (PMA) energy, which are essential for the state-of-the-art spintronic devices. The cubic HEOs with (001) orientation, with their fcc-based oxygen lattices, promise significant tunnel magnetoresistance (TMR) ratios due to the coherent tunneling [8–10] and strong interface PMA in Fe-based FMs due to the interfacial O 2*p*-Fe 3*d* orbital hybridization [11–13]. For practical applications, achieving PMA at an HEO/CoFeB (CFB) interface is essential because CFB is commonly used for perpendicularly magnetized MTJs due to the features such as a large TMR ratio, soft magnetic properties, and good compatibility with industrial sputter deposition processes. Furthermore, the structural stabilization and tunability of barrier properties by multicomponent cations offer considerable potential for innovation in the field of spintronics.

While MgO has historically been the barrier material of choice for MTJs [14,15], its application in meeting the requirements of spin-transfer torque (STT)-MRAM—where device dimensions must be shrunk below several tens of nanometers—reveals its limitations [16]. Such miniaturization for MTJs requires a significant reduction in *RA*, but reducing the thickness of insulating MgO barriers to less than 1 nm is extremely difficult. Therefore, the development of new barrier materials with low bandgaps (low barrier heights) while maintaining a large TMR ratio and a high breakdown voltage is urgently needed [17]. Recently, the exploration of a ternary oxide, $MgGa_2O_4$, as a low bandgap barrier has shown potential for improving a TMR ratio and reducing *RA* [18,19]. However, challenges remain in controlling atomic diffusion and ensuring the stability of the crystalline structure of the barrier layer. The integration of HEO barriers with more than five cations presents a promising avenue for achieving a stabilized crystal structure due to the large configuration entropy.

In this study, we report the development of atomically homogeneous cubic HEO epitaxial films with a LiTiMgAlGaO composition for interface PMA at a CFB FM interface and TMR effect in Fe/LiTiMgAlGaO/Fe-based MTJs. The HEO component was selected from the non-magnetic oxides with rock-salt-based or spinel-based oxide materials established as MTJ barriers with good insulator behavior: MgAl-O [20,21], LiMgAl-O [22], MgTi-O [23], and MgGa-O [18]. An increasing number of cation components in oxide materials will be advantageous for achieving structural stability while maintaining good insulating properties as a tunnel barrier. In addition, we developed an epitaxial growth technology to obtain high quality LiTiMgAlGaO thin films with atomic flatness and high (001) orientation. For the LiTiMgAlGaO epitaxial films for PMA, we developed an atomic-scale lamination technology based on radio frequency (RF) sputtering using LiTiO and MgAlGaO targets. Epitaxial growth with a rock-salt-like symmetrical crystal structure and an atomically flat surface was confirmed. The atomically homogeneous cation distributions across the films were also revealed, indicating that the stable formation of an ultra-thin HEO layer. The LiTiMgAlGaO/CFB stacks exhibited significant perpendicular magnetization, demonstrating that a large interface PMA energy is achieved by a chemically sharp interface of LiTiMgAlGaO with a CFB FM interface. Using RF sputtering of a $Li_{1/5}Ti_{1/5}Mg_{1/5}Al_{1/5}Ga_{1/5}O$ target, we developed an MTJ structure with Fe FM layers for observing TMR effect through the LiTiMgAlGaO barrier. We observed a relatively large TMR ratio of up to 84 % using an MTJ structure with Fe/LiTiMgAlGaO/Fe(001) with MgO nano-insertions. We also observed a small effective barrier height of 0.85–0.95 eV by the LiTiMgAlGaO barrier. These results demonstrate that the HEO materials have the potential to catalyze the advancement of low resistive MTJ barrier technology and provide essential insights into the next generation of materials engineering toward ultra-high density MRAMs and MTJ-based artificial intelligence (AI) devices.

Materials and methods

HEO-based film preparation using atomic-scale sputter lamination

Epitaxial cubic HEO(001) films were deposited on a single crystal MgO substrate using an ultra-high vacuum magnetron sputtering apparatus (EIKO Corporation) with a base pressure of less than 1×10^{-6} Pa. In this study, LiTiMgAlGaO (hereafter, L5O) films were developed as an HEO material using the atomic (0.3–0.5 nm) lamination of two spinel-based oxide materials, Li-Ti-O (LTO) and Mg-Al-Ga-O (MAGO), followed by post-annealing. Several different compositions of sintered oxide targets with a diameter of 76.2 mm are used for the L5O preparation: LTO = $Li_4Ti_5O_{12}$ ($Li_{44}Ti_{56}$-O) and $Li_{50}Ti_{50}$-O, and MAGO = $MgAlGaO_4$ ($Mg_{1/3}Al_{1/3}Ga_{1/3}$-O, hereafter, $Mg_{33}Al_{33}Ga_{33}$-O) and $Mg_{36}Al_{37}Ga_{27}$-O.

The detailed stack structure of the L5O films for structural analysis is MgO(001) substrate/[LTO (0.3 nm)/MAGO (t_{MAGO} = 0.3–0.5 nm)]$_n$ (total 10.2 ~ 20.4 nm), as shown in Fig. 1a. Prior to the deposition, the MgO substrate was cleaned by *in-situ* annealing at 600 °C. The lamination films were deposited by the RF power for LTO (MAGO) 50 or 100 W (100 W) with an Ar pressure of 1.33 Pa at room temperature (RT). Typical deposition rates for LTO and MAGO are between 0.02 and 0.03 nm/s. The L5O composition was tuned by the target compositions and t_{MAGO} to obtain a relative equimolar composition for high configuration entropy. The deposited L5O films were annealed *in-situ* at 400 °C for 15 min to promote the cation mixing and improve the crystallinity. Reflection of high-energy electron diffraction (RHEED) was used to evaluate the surface crystal structure. The surface morphology was evaluated by atomic force microscopy (AFM) after deposition. Reference 10 nm thick LTO and MAGO films were also deposited on a single crystal MgO substrate by RF sputtering. Using X-ray reflectometry (XRR), the densities of the reference LTO and MAGO films were estimated to be 4.08 and 5.02 g/cm^3, respectively.

Inductively coupled plasma optical emission spectroscopy (ICP-OES) was used to determine the compositions of cation elements of ~ 100 nm thick films deposited on thermally oxidized Si substrate at RT from the targets, $Li_{44}Ti_{56}$-O, $Li_{50}Ti_{50}$-O, $Mg_{33}Al_{33}Ga_{33}$-O, and $Mg_{36}Al_{37}Ga_{27}$-O; the compositions were determined to be Li:Ti = 44.9:55.1 atm%, Li:Ti = 33.4:66.6 atm%, Mg:Al:Ga = 34.6:29.2:36.2 atm%, and Mg:Al:Ga = 36.9:32.8:30.3 atm%, respectively. The higher Ti composition in the film from the $Li_{50}Ti_{50}$-O target than that of the $Li_{44}Ti_{56}$-O target may be due to the difference in the target density. We calculated the nominal compositions of L5O using the ICP-OES compositions and XRR film densities of LTO and MAGO. The calculated nominal compositions of L5O single-layer films using the ICP-OES data are listed in Table. 1.

PMA film preparation

Multilayer films with a structure of MgO(001) substrate/[$Li_{50}Ti_{50}$-O (0.3)/$Mg_{36}Al_{37}Ga_{27}$-O (0.4)]$_{15}$ (10.5)/$Co_{20}Fe_{60}B_{20}$ (CFB) (t_{CFB} = 0.7 – 1.7)/W (0.3)/Ta (5), (numbers in parentheses in nm) were prepared, as shown in Fig. 1b. Prior to the CFB deposition, the L5O surface was exposed to a pure O_2 gas (99.999 %, ~ 5 Pa) for 300 s in the sputtering chamber at RT to tune the L5O interface [19,24]. Note that this oxidation process is sufficiently weak and therefore does not significantly change the L5O surface structure or the magnetic properties of the CFB layer. After the deposition, the film stacks were annealed *ex-situ* at T_{AN} = 250 °C, 300 °C, and 350 °C to promote a PMA at the L5O/CFB interface.

Characterization of films

The crystal structure of the L5O films was characterized by out-of-plane XRD (scattering vector q//MgO[001] and q//MgO[111]) 2θ-ω scans with Cu $K_{\alpha 1}$ radiation and an incident Ge(220) monochromator (SmartLab HyPix-3000, Rigaku Corporation). In addition, out-of-plane q//MgO[111] scans are evaluated at angles of χ = 54.7°, and φ = 45.0°. The microstructure analysis of annular dark-field (ADF-) STEM observation, and nano-beam electron diffraction (NBED) with energy dispersive X-ray spectroscopy (EDS) was carried out at 200 kV accelerating voltage using Titan G2 80–200 and Spectra Ultra S/TEM (Thermo Fisher Scientific). To guarantee the quality of STEM investigation, a 50-nm-thick STEM lamellae were prepared by a thickness-controllable technique based on backscattered electrons (BSEs) intensity using focused-ion-beam (FIB)-scanning electron microscopy (SEM) dual-beam

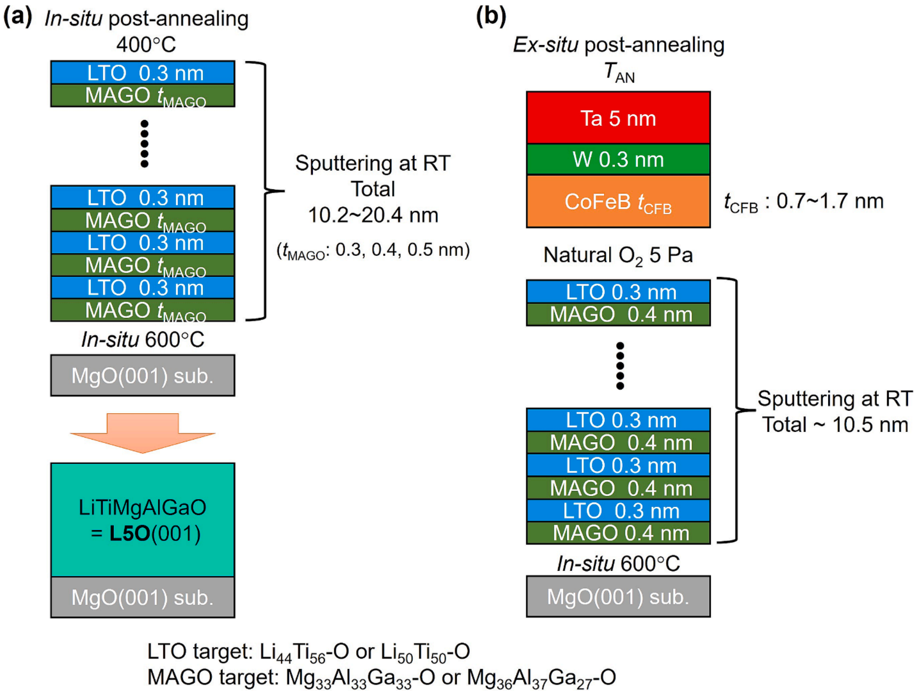

Fig. 1. Schematic illustration of L5O film stacks. (a) Stacking for single-layer L5O films. (b) Stacking for interface PMA samples.

Table 1

Summary of nominal compositions of L5O films determined by ICP-OES and STEM-EDS in atomic %. * for Li: the value calculated using the Li/Ti ratio (0.815) of the ICP-OES result.

Sample	Thickness (nm)	Method	Targets, stack design (nm)	Li	Ti	Mg	Al	Ga
A	10.2 (design)	ICP	$Li_{44}Ti_{56}$-O 0.3	23	29	18	15	15
	12.7 (STEM)	EDS + ICP(Li)	/$Mg_{33}Al_{33}Ga_{33}$-O 0.3	27*	33	15	12	14
B	20.4 (design)	ICP	$Li_{50}Ti_{50}$-O 0.3 /$Mg_{36}Al_{37}Ga_{27}$-O 0.3	16	32	19	17	16
C	20.3 (design)	ICP	$Li_{50}Ti_{50}$-O 0.3 /$Mg_{36}Al_{37}Ga_{27}$-O 0.4	14	28	20	19	18
D	20.0 (design)	ICP	$Li_{50}Ti_{50}$-O 0.3 /$Mg_{36}Al_{37}Ga_{27}$-O 0.5	12	24	24	21	19
MTJ	1.9 (design)	ICP	$Li_{20}Ti_{20}Mg_{20}Al_{20}Ga_{20}$-O	26	13	23	18	20

Helios5UX equipped with Auto Script (Thermo Fisher Scientific) [25]. Lithium (Li) cannot be detected by EDS in principle; thus, atom probe tomography (APT) was carried out to analyze the Li distribution by using Invizo6000 (AMETEK) in the 440 kHz laser pulsing mode with 50 pJ energy at the specimen temperature of 30 K. X-ray photoemission spectroscopy (XPS) was used (Quantes, ULVAC-PHI, Inc.) to obtain the chemical states of each cation in the films; XPS profiles were recorded using Al K_α monochromatic X-rays of 25 W and 100 μm in diameter. The magnetic properties of the L5O/CFB structures were characterized using a vibrating sample magnetometer (VSM) at RT.

L5O-based MTJ preparation and magnetotransport measurements

To investigate the magnetotransport properties, MTJs with an ultrathin LiTiMgAlGaO barrier were prepared using RF sputtering of a LiTiMgAlGaO single sintered target instead of the multilayer of the LTO and MAGO layers. The MTJ multilayer structure is MgO(001) substrate/Cr buffer (60)/bottom-Fe (50)/bottom-MgO ($t_{\text{Bot-MgO}} = 0$–1 nm)/$Li_{1/5}Ti_{1/5}Mg_{1/5}Al_{1/5}Ga_{1/5}O$ (t_{L5O})/top-MgO (0.3)/top-Fe (5)/$Ir_{20}Mn_{80}$ (IrMn) (10)/Ru (10), (numbers in parentheses in nm), as shown in Fig. 10a. Using ICP-OES, the composition of cation elements of a 100 nm thick film from the $Li_{1/5}Ti_{1/5}Mg_{1/5}Al_{1/5}Ga_{1/5}O$ target was determined to be $Li_{26}Ti_{13}Mg_{23}Al_{18}Ga_{20}$-O. The bottom- and top-MgO layers were inserted to improve the Fe/L5O interface states as used for the Fe/$MgGa_2O_4$/Fe MTJs [19]. The $t_{\text{Bot-MgO}}$ and t_{L5O} were varied within a 20 mm width wafer during deposition using a linear motion shutter. Since we used the thick Fe layers, the MTJs were obtained as an in-plane magnetization type. Each layer was deposited by DC or RF magnetron sputtering at RT and post-annealed *in-situ* for 15 min to improve the flatness and crystallinity. After post-annealing of the L5O layer at 350 °C, the L5O surface was exposed to a pure O_2 gas for 300 s at RT, similar to the PMA sample. After the deposition, the multilayer was post-annealed *ex-situ* using a vacuum annealing system (base pressure ~ 10^{-5} Pa) at 200 °C for 30 min under a 2 kOe magnetic field application along Fe[100] to exchange bias the top-Fe layer.

A prepared MTJ multilayer was patterned into 8 × 8 or 12 × 12 μm^2 squared MTJs using maskless lithography, photolithography, and Ar ion milling. Magnetotransport properties were characterized by DC four probe method at RT using a Keithley 2400 sourcemeter and a Keithley 2182A nanovoltmeter. A TMR ratio (%) was defined as $100\times(R_{AP} - R_P)/R_P$, where R_{AP} (R_P) indicates tunneling resistance for the parallel, P (antiparallel, AP) magnetization state of the Fe layers.

Results and discussion

Surface and crystal structures

Fig. 2a shows the AFM image of the surface of a 20-nm-thick L5O film with a design of [$Li_{50}Ti_{50}$-O 0.3 nm/$Mg_{36}Al_{37}Ga_{27}$-O $t_{\text{MAGO}} = 0.4$ nm]$_n$ (Sample C, calculated composition: $Li_{0.14}Ti_{0.28}Mg_{0.20}Al_{0.19}Ga_{0.18}$-O). An atomically flat surface of the L5O film was achieved with an average

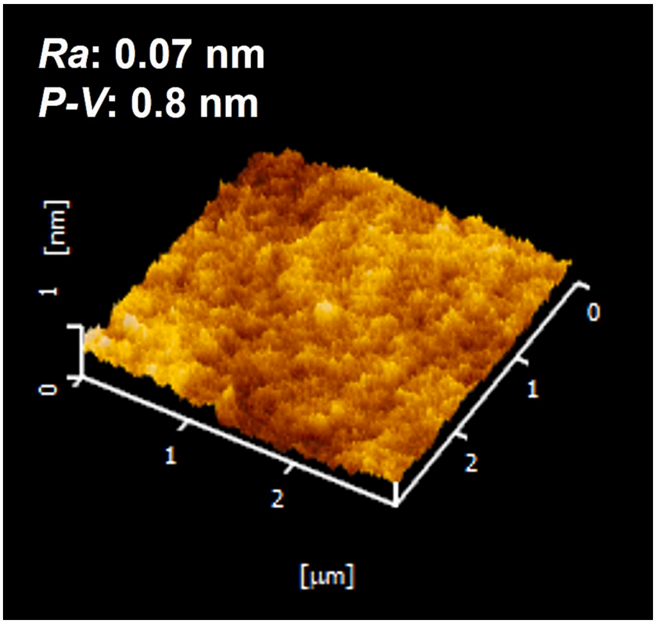

Fig. 2. AFM image of the L5O film. Surface morphology of 20-nm-thick film with a design of $[Li_{50}Ti_{50}$-O 0.3 nm/$Mg_{36}Al_{37}Ga_{27}$-O $t_{MAGO} = 0.4$ nm$]_n$ (Sample C), 3 × 3 μm^2 scan.

roughness (*Ra*) of 0.07 nm (≪ one monolayer of L5O ~ 0.2 nm) and a peak-to-valley (*P-V*) of 0.8 nm, which is suitable for MTJ applications.

Fig. 3 shows the RHEED patterns of 20-nm-thick L5O films with designs of $[Li_{50}Ti_{50}$-O 0.3 nm/$Mg_{36}Al_{37}Ga_{27}$-O $t_{MAGO}]_n$: a, $t_{MAGO} = 0.4$ nm with electron-beam along the MgO[100] azimuth (Sample C) and b, $t_{MAGO} = 0.5$ nm along the MgO[110] azimuth (Sample D, calculated composition: $Li_{0.12}Ti_{0.24}Mg_{0.24}Al_{0.21}Ga_{0.19}$-O). Both the L5O layers show epitaxial growth with (001) orientation. The pattern of Sample C shows sharper spots with additional diagonal line structures (Kikuchi lines), indicating better surface crystallinity of Sample C than that of Sample D. Due to the absence of the spinel supper lattice streak, a rock-salt-like structure (cation-disordered spinel) [26,27] is obtained for both the samples, resulting in half the unit cell size of an ordered spinel structure (lattice constant ~ 0.4 nm). This cation-disorder behavior was also reported in $MgAl_2O_4$ and $MgGa_2O_4$ barriers [19,28]. There are no additional spots or streaks in the patterns; the L5O has a single-phase structure without any secondary phases.

Fig. 4a (Fig. 4d) shows the out-of-plane XRD pattern of 10-nm thick L5O films with a design of $[Li_{44}Ti_{56}$-O 0.3 nm/$Mg_{33}Al_{33}Ga_{33}$-O 0.3 nm$]_n$ (Sample A, $Li_{0.23}Ti_{0.29}Mg_{0.18}Al_{0.15}Ga_{0.15}$-O), in the *q*//[001] direction (*q*//[111] direction). The patterns of 10 nm thick $Li_4Ti_5O_{12}$ (LTO) and 10 nm thick $Mg_{33}Al_{33}Ga_{33}O$ (MAGO) films grown on a MgO(001) substrate are also shown in the plots as references. In the *q*//[001] direction, the Bragg reflections corresponding to the (004) and (008) planes (indices for a spinel lattice) are observed for the LTO and MAGO reference layers. The L5O film shows peaks near the LTO or MAGO, indicating that a cubic HEO film was achieved. As can be clearly seen in the close-ups of the *q*//[001] scans (Fig. 4b and 4c), the peak intensities

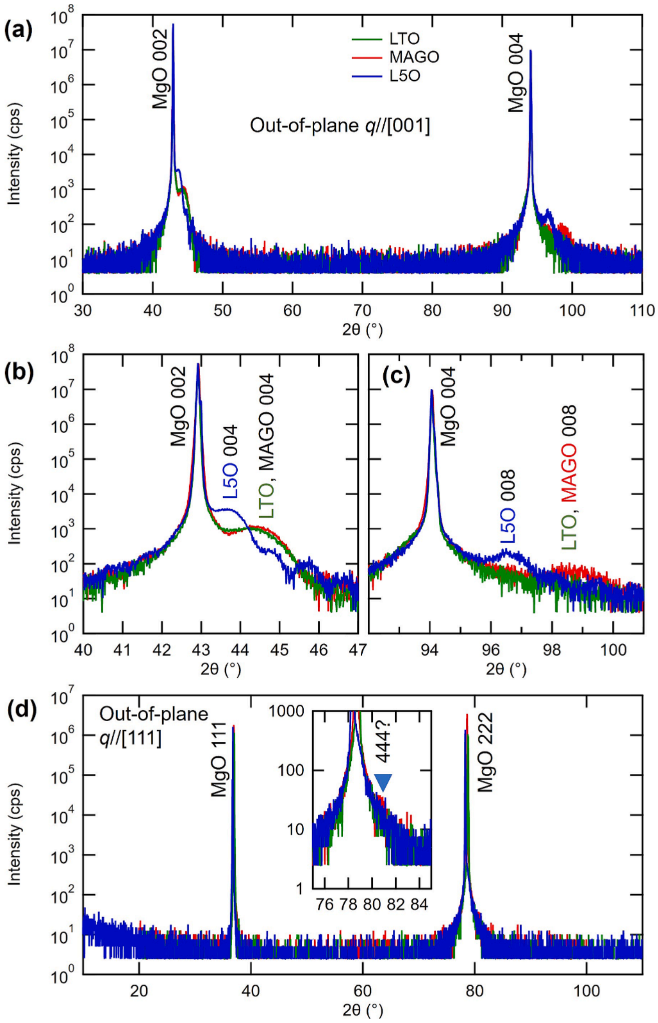

Fig. 4. Out-of-plane XRD scans of 10 nm thick L5O, $Li_4Ti_5O_{12}$ (LTO), and $Mg_{33}Al_{33}Ga_{33}O$ (MAGO) films. (a)-(c) Profiles in the scattering vector *q*// [001] direction and (d) *q*//[111] direction for 10-nm thick film with a design of $[Li_{44}Ti_{56}$-O 0.3 nm/$Mg_{33}Al_{33}Ga_{33}$-O 0.3 nm$]_n$ (Sample A), LTO, and MAGO films. (c) and (b) Close-ups near 004 and 008 peaks, respectively. The indices are for an ordered spinel lattice. Inset of (d) is a close-up near the MgO 222 peak.

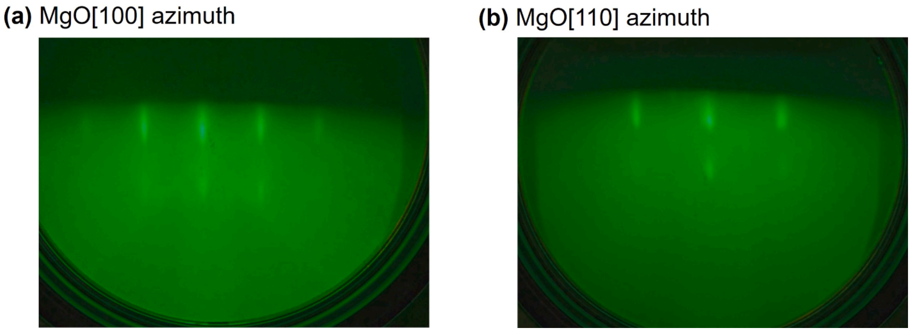
(a) MgO[100] azimuth

(b) MgO[110] azimuth

Fig. 3. RHEED patterns of L5O films. $[Li_{50}Ti_{50}$-O 0.3 nm/$Mg_{36}Al_{37}Ga_{27}$-O $t_{MAGO}]_n$ with (a) $t_{MAGO} = 0.4$ nm (Sample C) and (b) $t_{MAGO} = 0.5$ nm (Sample D) after post-annealing at 400 °C.

of L5O, i.e., L5O(004) and L5O(008), are several times higher than those of LTO and MAGO, suggesting that the crystallinity is improved by the use of five cationic elements. The L5O peak positions are shifted to the lower 2θ angles from the LTO and MAGO positions, indicating the increase in the out-of-plane lattice spacing from the LTO and MAGO parent compounds. Only the L5O film shows clear interference oscillations near the Bragg positions (e.g., ~44.8°, ~45.7°, etc.), indicating flat film formation as seen in the AFM image (Fig. 2). Only 00*L* reflections are observed from these films, indicating that L5O, LTO, and MAGO are epitaxially grown with (001) orientation. Therefore, an atomically homogeneous L5O film was synthesized by our atomic alternative sputtering using LTO and MAGO due to the significant atomic mixing between the layers during the sputtering process. In the $q//[111]$ scans, the reflections from the films almost overlap with the MgO 111 and MgO 222 substrate peaks, as seen in the inset of Fig. 4d. The absence of reflections from (*LLL*), L = odd, indicates the formation of the cation disorder spinel structure instead of an ordered spinel structure, consistent with the RHEED observation. The formation of the cation-disordered spinel structure can be attributed to our process temperatures (~400 °C), which are much lower than the melting points of the parent compounds (≫1500 °C). Using the $q//[001]$ scan, the out-of-plane lattice constant c_{L5O} of the L5O was determined to be ~ 0.414 nm.

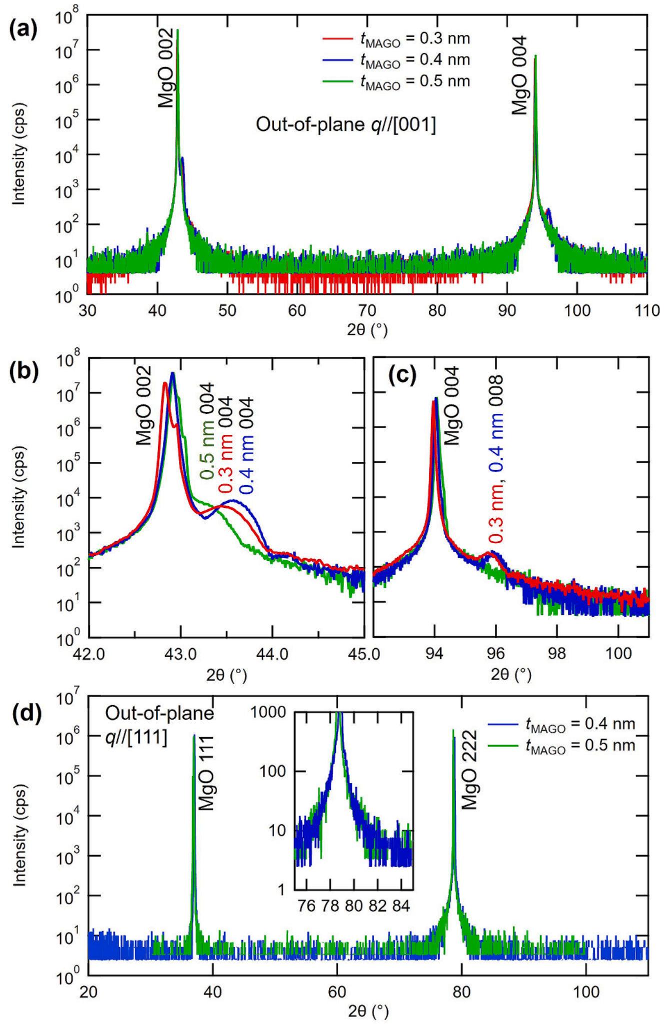

Fig. 5. Out-of-plane XRD scans of 20 nm thick L5O films with different MAGO thicknesses. (a)-(c) Profiles with a scattering vector $q//[001]$ direction and (d) $q//[111]$ direction for $[\mathrm{Li_{50}Ti_{50}}$-O 0.3 nm/$\mathrm{Mg_{36}Al_{37}Ga_{27}}$-O $t_{\mathrm{MAGO}} = 0.3$, 0.4, 0.5 nm$]_n$ (Sample B, Sample C, and Sample D, respectively). (c) and (b) Close-ups near LTO 004 and 008 peaks, respectively. The indices are for an ordered spinel lattice. Inset of (d) is a close-up near the MgO 222 peak.

Fig. 5a (Fig. 5d) shows the out-of-plane XRD patterns in the $q//[001]$ direction ($q//[111]$ direction) of 20 nm thick L5O films with different L5O compositions. The design structures are $[\mathrm{Li_{50}Ti_{50}O}$ (0.3)/$\mathrm{Mg_{36}Al_{37}Ga_{27}O}$ $t_{\mathrm{MAGO}}]_n$ with $t_{\mathrm{MAGO}} = 0.3$ nm (Sample B, calculated composition: $\mathrm{Li_{0.16}Ti_{0.32}Mg_{0.19}Al_{0.17}Ga_{0.16}}$-O), 0.4 nm (Sample C), and 0.5 nm (Sample D). The three films show epitaxial growth with (001) orientation and have a single phase of a cation-disorder structure, similar to Sample A (Fig. 4). No secondary phases were observed within the compositional range of the films. The noticeable peak shifts of L5O 004 and L5O 008 were observed with t_{MAGO}. The highest L5O peak intensities were observed for $t_{\mathrm{MAGO}} = 0.4$ nm, indicating the improved L5O crystallinity due to the near equimolar composition of five elements achieved for this sample.

Cross-sectional STEM analysis

The results of the cross-sectional microstructural analysis using STEM of the 10 nm thick L5O (Sample A) and the PMA sample with t_{CFB} = 1.0 nm are shown in Fig. 6. Fig. 6a shows the low magnification ADF-STEM image of Sample A. The flat surface and the sharp interface with the MgO substrate are observed. The actual film thickness is ~ 12.7 nm, which is slightly thicker than the design thickness of 10 nm of a sum of the LTO and MAGO thicknesses. This may be due to the accuracy of the sputtering shutter motion for ultra-thin layers for each step (0.3–0.5 nm, corresponding to a deposition time of a few to more than ten seconds) and the change in the film density during the formation of an L5O compound by the processes. The high magnification ADF-STEM image in Fig. 6b shows the formation of high-quality epitaxial (001) growth of the L5O lattice on the MgO(001) lattice. We also found that the MgO substrate completely locks the in-plane lattice of the L5O film, resulting in perfect lattice matching between MgO and L5O. As shown in Fig. 6e, there were no misfit dislocations at the interface, as can be seen in the inverse fast Fourier transform (IFFT) STEM image by selecting (200) and $(\bar{2}\,00)$ diffraction spots from the FFT-filtered Fig. 6b image (in-plane lattice constant $a_{\mathrm{MgO}} \sim a_{\mathrm{L5O}} \sim 0.421$ nm). Therefore, the L5O is slightly tetragonally distorted ($c_{\mathrm{L5O}}/a_{\mathrm{L5O}} \sim 0.98$). The similar NBED patterns shown in Fig. 6c and 6d obtained from and the L5O layer and the MgO substrate, respectively, indicate the good crystallinity of the L5O film. Although the NBED pattern has very weak {022} spinel superlattice reflections as indicated by the yellow circle, the L5O film nominally has a cation-disordered spinel structure, as expected from the XRD results.

The EDS elemental maps of each element are shown in Fig. 6f–6k. Note that Li cannot be detected by our EDS technique. Homogeneous atomic distributions of Ti, Mg, Ga, Al, and O without any clustering were confirmed throughout the 10 nm film. Additionally, no significant interdiffusion to the MgO substrate was observed, indicating that stable formation of the single-phase L5O film. Fig. 6l shows the EDS line profiles, which shows that the film is Ti rich due to the higher composition of Ti than Mg, Ga, and Al in the ICP-OES estimation of $\mathrm{Li_{0.23}Ti_{0.29}Mg_{0.18}Al_{0.15}Ga_{0.15}}$-O. Note that the O signal level is higher than the actual composition since Li atoms in L5O are not included in the profiles. The slight segregation of Mg at the surface may be due to air exposure of the film during the STEM sample preparation. As shown in Table 1 for Sample A, the differences between the calculated composition using the ICP-OES and the EDS compositions (assuming the Li composition using the ICP-OES Li/Ti ratio) are small. These microstructural analyses indicate the formation of epitaxial growth of HEOs obtained by the alternating sputtering method at relatively low process temperatures up to 400 °C.

Fig. 6m presents the low magnification ADF-STEM image of the interface PMA sample with the stack design of [LTO (0.3)/MAGO (0.4)$]_{15}$ (10.5)/CFB ($t_{\mathrm{CFB}} = 1.0$)/W (0.3)/Ta (5), (numbers in parentheses in nm) with $T_{\mathrm{AN}} = 250$ °C. The flat surface of the L5O layer is consistently observed with the AFM and XRD results in Fig. 2 and Fig. 4. Fig. 6n provides the high magnification image near the L5O/CFB interface. The sharp interface with the CFB layer is observed without any

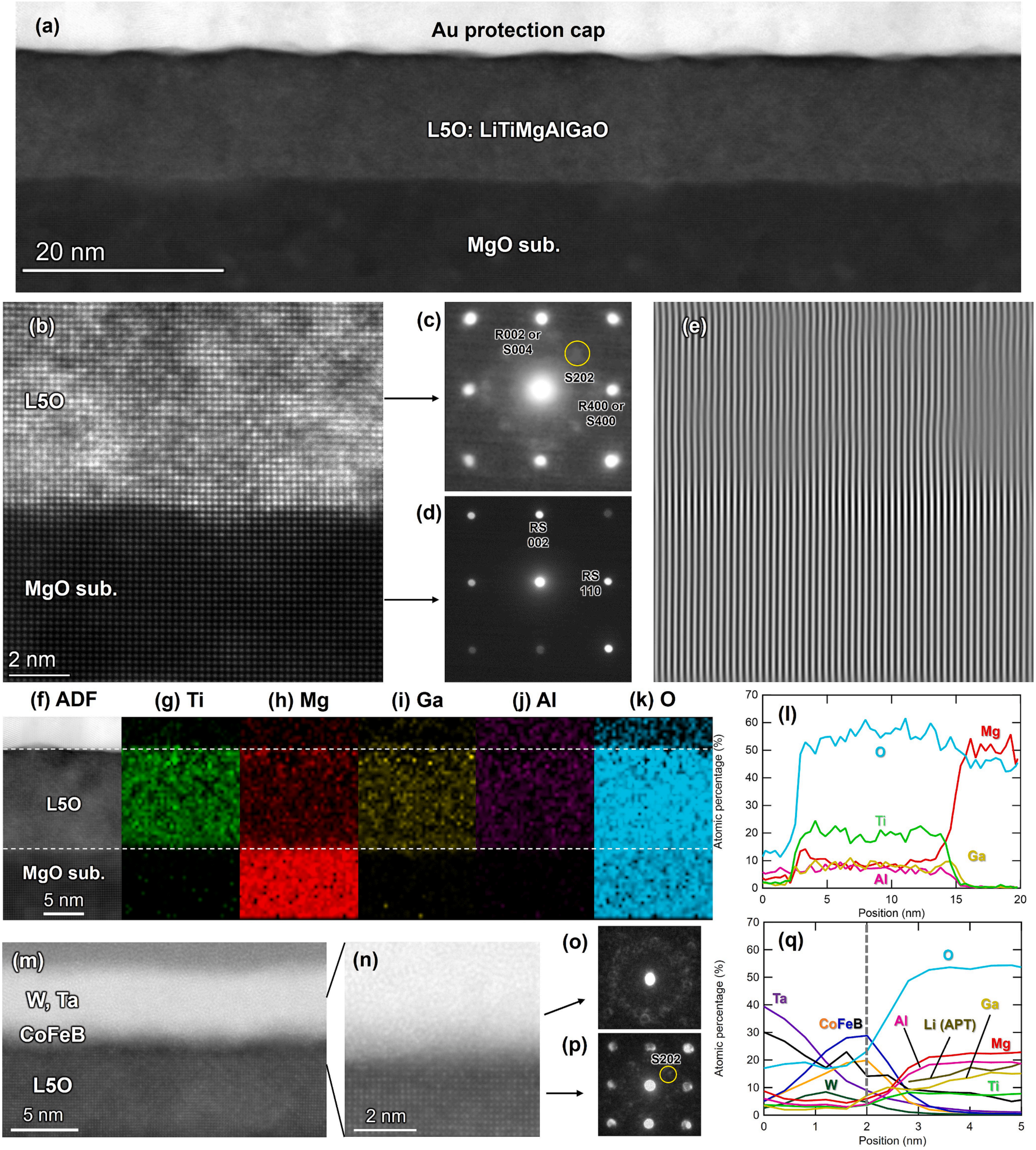

Fig. 6. STEM analysis of cross-section of single L5O film and L5O/CFB stack. (a) Low magnification and (b) high magnification ADF-STEM images of the 10 nm thick L5O film (Sample A). (c),(d) NBED patterns taken from (c) MgO substrate and (d) L5O. "R" and "S" in (c) and (d) indicates a rock-salt structure (spinel structure) and spinel structure. Yellow circle in (c) and (p) indicates one spinel superlattice spot (202). (e) IFFT STEM image by selecting (200) and $(\bar{2}00)$ diffraction spots of the FFT filtered image of (b). (f)-(k) EDS maps for (f) ADF image, (g) Ti, (h) Mg, (i) Ga, (j) Al, and (k) O. (l) Corresponding EDS profiles of Sample A. (m) Low magnification ADF-STEM images of L5O/CFB stack. (n) Higher magnification image near L5O/CFB interface. (o),(p) NBED patterns taken from (o) CFB and (p) L5O. (q) Corresponding EDS profiles of L5O/CFB stack. The result of Li composition by APT was added to the elemental compositional line profile, indicated as "Li (APT)".

segregation. The NBED patterns of the L5O and CFB layers are shown in Fig. 6o and 6p, respectively. The patterns indicate the good crystallinity of the L5O film and an amorphous structure of the CFB layer. The NBED pattern shows weak {022} spinel superlattice reflections (yellow circle), however, the L5O film almost possesses a cation-disordered spinel structure, consistent with Sample A and the XRD profiles. Moreover, Fig. 6q shows the EDS line profiles and APT profile of Li around the L5O/CFB interface. No significant interdiffusion is found near the interface.

XPS analysis

Fig. 7 depicts XPS profiles of the 10 nm thick L5O film (Sample A): Mg1s (Fig. 7a), Ga2p3 (Fig. 7b), O1s (Fig. 7c), Ti2p3 (Fig. 7d), Al2p (Fig. 7e), and Li1s (Fig. 7f), confirming the presence of the five metal oxides near the surface region of the L5O film even after the 400 °C annealing. The XPS results were calibrated using the C1s spectrum, as shown in Supplementary S1 and Fig. S1. The fitting employs the convolution of Gaussian and Lorentzian function (cyan line) and the Shirey background (black dashed line). The spectrum data for each element is well-fitted (cyan line and red dot). The spectrum has been

Table 2
Summary of XPS analysis for L5O components.

Orbital	Binding energy (eV)	Materials	Oxidation state
Mg1s	1303.71	MgO	2+
Ga2p3	1117.89	Ga_2O_3	3+
O1s	530.20	MgO, Ga_2O_3 TiO_2, Ti_2O_3 Al_2O_3, LiOH	2−
	532.15	C-O	2−
Ti2p3	458.64	TiO_2	4+
	457.20	Ti_2O_3	3+
Al2p	73.93	Al_2O_3	3+
L1s	54.82	LiOH	1+

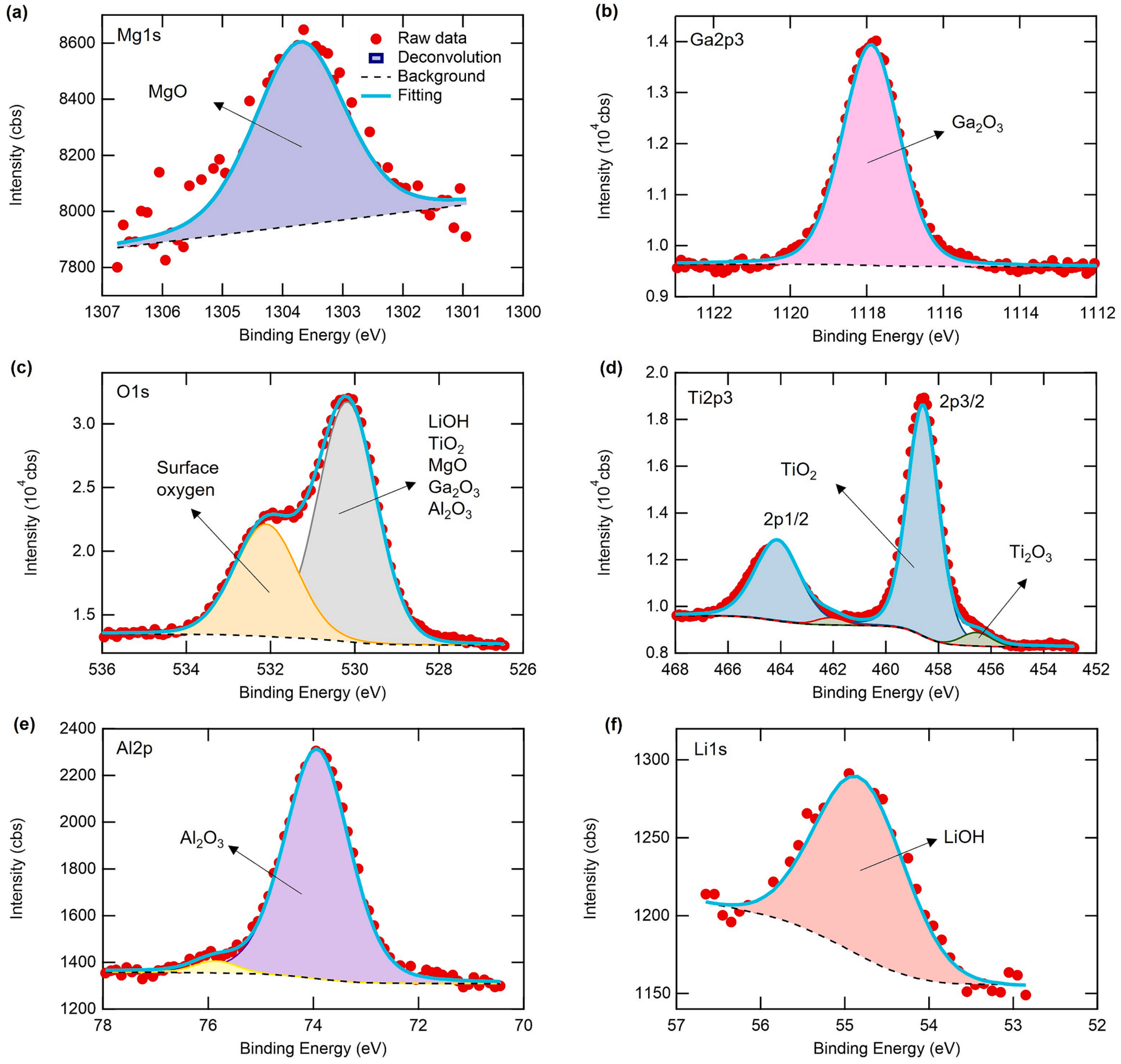

Fig. 7. XPS spectra of the L5O film. (a) Mg1s, (b) Ga2p3, (c) O1s, (d) Ti2p3, (e) Al2p, and (f) Li1s of the L5O film (Sample A).

deconvoluted into its constituent elements and compared to the database [29]. Table 2 provides a summary of binding energies and oxidation states.

Magnesium has an oxidation state of 2+ and a binding energy of 1303.71 eV. The binding energy of magnesium is comparable to that reported in a prior work [30]. Gallium and aluminum have the same oxidation state (3+), with binding energies of 1117.89 eV and 73.93 eV, respectively. The binding energies of Ga and Al are consistent with those reported in a recent work [31,32]. The deconvoluted peaks of the O1s spectrum in Fig. 7c are attributed to the C-O bond (532.15 eV) and oxide ions (530.20 eV) in the lattice. The symmetric peak at 530.20 eV represents the oxidation state of 2− for oxygen. The binding energy of O1s was like that found in a previous work [31]. The additional peak of O1s is attributed to the surface oxygen produced by the reaction of oxygen with air, such as carbon and oxygen (surface oxygen) [33]. Two oxidation states, 4+ and 3+, are observed in the Ti $2p_{3/2}$ peak, with binding energies of 458.64 eV and 457.20 eV, respectively. The binding energies of Ti4+ and Ti3+ are comparable to those found in previous work [34,35]. The ratio of Ti4+ area to Ti3+ area is more than ten times, indicating that Ti4+ is the primary contributor. Lithium has an oxidation state of 1+ and a binding energy of 54.82 eV, according to lithium hydroxide (LiOH) [36]. The absence of a capping layer in the film causes the formation of LiOH. However, the O1s from LiOH had a binding energy of 530.20 eV (Fig. 7c), confirming the presence of lithium hydroxide. The above analysis indicates that the L5O thin film contains little unoxidized metals and is formed as a homogeneous oxide layer.

PMA properties at L5O/CFB interfaces

Fig. 8 shows the in-plane (IP) and out-of-plane (OOP) magnetization as a function of a magnetic field for the stack design of [LTO (0.3)/MAGO (0.4)]$_{15}$ (10.5)/CFB ($t_{CFB} = 0.8$–1.3)/W (0.3)/Ta (5), (numbers in parentheses in nm) with $T_{AN} = 250$ °C. The sample with $t_{CFB} = 0.8$ nm (Fig. 8a) shows low saturation magnetization and isotropic anisotropy due to the contribution of the large magnetic dead layer formed mainly at the W interface, as shown next. In contrast, the samples with $t_{CFB} =$ 1.0 and 1.1 nm clearly show perpendicular magnetization due to the atomically flat L5O interface: magnetically easy for the OOP loops and hard for the IP loops (Fig. 8b and 8c). The perpendicular magnetization is also observed after annealing of $T_{AN} = 350$ °C for $t_{CFB} = 1.0$ and 1.1 nm, as shown in Supplementary S2 and Fig. S2. Therefore, the L5O(001) interface can induce large PMA at the FM interface. In addition, the L5O/CFB has a chemically sharp interface, as shown in Fig. 6n, resulting in a considerable interface PMA energy, K_{eff}. The origin of the interface PMA is expected to be the promotion of the interfacial hybridization of O-Fe orbitals, as reported in the oxide/Fe-based FM interfaces such as MgO/Fe [12], cation-disordered $MgAl_2O_4$/Fe [37], and NiO/Fe [38]. Further experiments, such as X-ray magnetic circular dichroism [13,39], will be required to clarify the microscopic origin. These PMA properties demonstrate that L5O is a good candidate for the barrier for perpendicularly magnetized MTJs (pMTJs). The sample with a thicker $t_{CFB} =$ 1.3 nm (Fig. 8d) shows in-plane magnetization due to the increase in the shape anisotropy contribution [11].

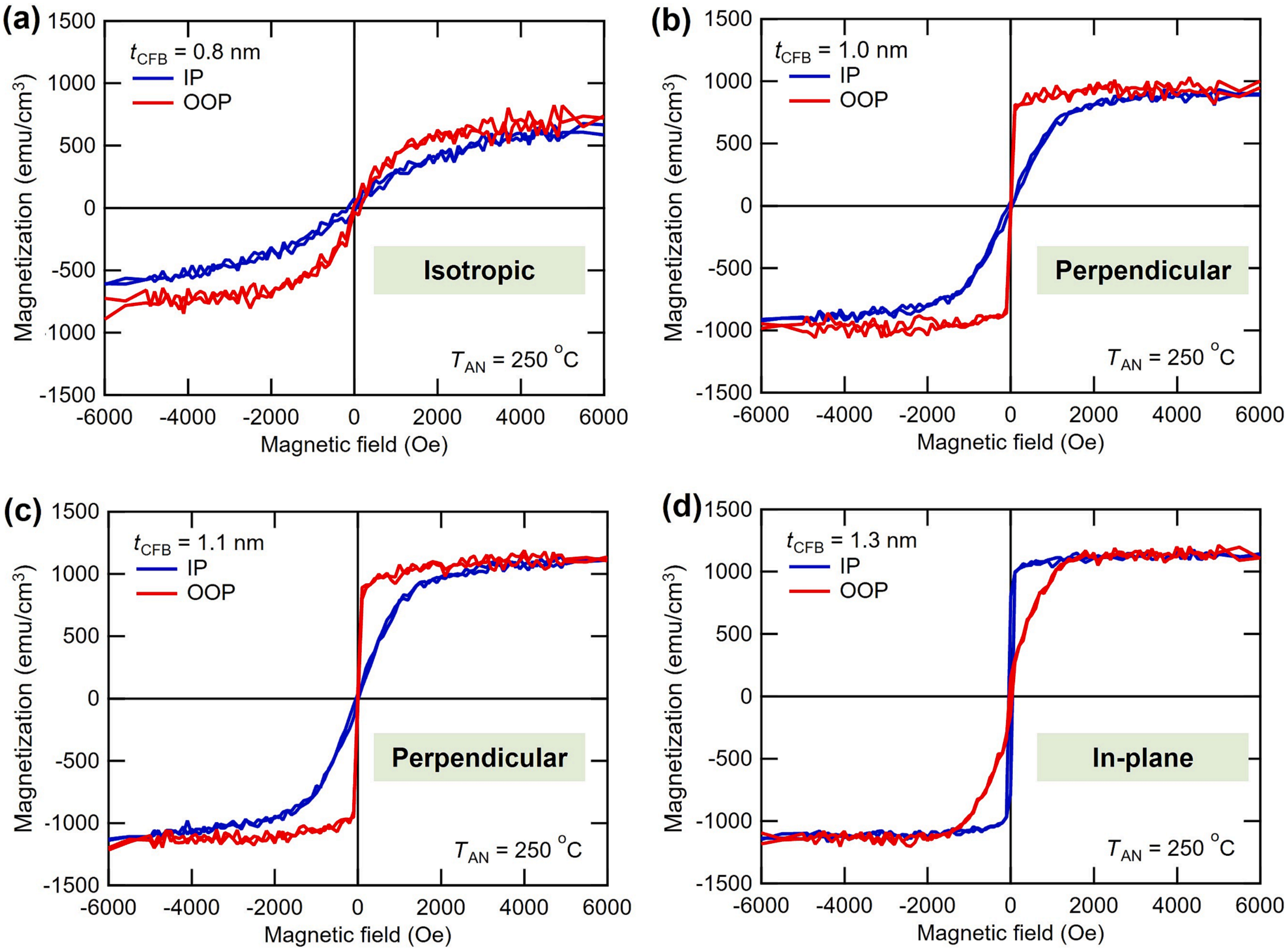

Fig. 8. Magnetization (*M*−*H*) curves of L5O/CFB stacks. (a)-(d) IP and OOP *M*−*H* curves of L5O/CFB (t_{CFB}) stacks after $T_{AN} = 250$ °C. (a) $t_{CFB} = 0.8$ nm, (b) 1.0 nm, (c) 1.1 nm, and (d) 1.3 nm.

Fig. 9a plots the magnetic moments per unit area as a function of t_{CFB} with $T_{AN} = 250$ °C, 300 °C, and 350 °C. The solid lines are the results of the linear fits. The x-axis intercepts of the linear fits indicate the magnetic dead layer thickness $t_{MD} = 0.5$ nm and 0.6 nm for $T_{AN} = 250$ °C and 300 °C, respectively. The intrinsic saturation magnetization after subtracting the effect of t_{MD} (M_s) can be determined from the slope of the fits. We obtain intrinsic M_s of 1880 (1950) emu/cm^3 for $T_{AN} = 250$ °C (300 °C). The intrinsic M_s values are similar to those reported for CFB/MgO PMA structures after post-annealing [40], and are close to the M_s of Co-Fe alloys due to B diffusion of CFB to the W side. The intrinsic M_s and t_{MD} are almost the same as those observed in the MgO/CFB systems [41], indicating that the L5O/CFB interface has a similar sharpness. The nonlinear relationship was observed for $T_{AN} = 350$ °C, which may indicate that the interdiffusion of elements becomes more significant.

To extract the interfacial contribution of the PMA of the L5O/CFB, we evaluated the effective CFB thickness ($t' = t_{CFB} - t_{MD}$) dependence of $K_{eff} \cdot t'$, where K_{eff} is the volume PMA energy, which was calculated using the area enclosed by IP and OOP magnetization loops. The interface PMA energy is calculated by the relationship: $K_{eff} \cdot t' = \left(K_V - 2\pi M_S^2\right)t' + K_i$, where K_V is the bulk magnetocrystalline anisotropy energy density, and $-2\pi M_S^2$ is the shape anisotropy energy density, respectively (in CGS units). In Fig. 9b, the y-intercepts correspond to the K_i values, which are determined to be 0.8 erg/cm^2 for $T_{AN} = 250$ °C and 300 °C. Although the positive K_{eff} is observed for $T_{AN} = 350$ °C, the $K_{eff} \cdot t'$ plot shows a deviation from the linear line due to interdiffusion. The deviations at the low t' regions for all the plots are typically observed in interface PMA systems [40,42–44]. A magnetoelastic contribution due to the lattice mismatch with an FM layer will also be the origin of such a deviation [45]; however, it is not significant in our L5O/CFB interfaces since the CFB layers are nearly amorphous as shown in Fig. 6m–6p.

Although the K_i values do not exceed the MgO/CFB interface (1.3 erg/cm^2) [11], our interface PMA results show the applicability of HEOs for interfacial functionality such as spintronic devices. Interface modifications, such as the nano-layer insertion, as shown in the following section, and tuning the oxidation state of the barrier [46], will lead to an improvement of the PMA energy.

TMR properties of Fe/L5O/Fe(001) MTJs

Fig. 10b shows the RHEED patterns for the MgO[100] azimuth at each growth stage for the MTJ stack of Fig. 10a. The patterns for the MgO[110] azimuth were shown in Supplementary S3 and Fig. S3. All patterns show clear streaks, and different patterns are obtained for the [100] and [110] azimuths, indicating epitaxial growth from the bottom-Fe to the top-Fe with (001) orientation. The bottom-Fe[100] pattern has additional streaks marked with red arrows due to oxygen adsorption during the post-annealing [19]. The bottom-MgO and top-MgO show similar patterns, indicating their (001)-oriented rock-salt structure with 45° in-plane lattice rotation on the bottom-Fe. The pattern of the L5O layer also shows highly (001)-oriented epitaxial growth due to the good lattice matching between MgO and L5O, as shown in Fig. 6e. The crystal structure is also the cation-disordered spinel structure due to the absence of the superlattice streak, similar to Fig. 3. Therefore, we obtained an MgO/L5O/MgO barrier between high quality Fe(001) FM electrodes using sputtering method.

The $t_{Bot\text{-}MgO}$ dependences of the TMR ratios and RA values (bias voltage ~ 10 mV) of the MgO/L5O/MgO MTJs with $t_{L5O} = 1.75$ nm at RT are shown in Supplementary S4 and Fig. S4. The TMR ratio increases with $t_{Bot\text{-}MgO}$ and reaches 80 % at $t_{Bot\text{-}MgO} = 0.45$ nm. Fig. 10c shows the TMR ratio as a function of the in-plane magnetic field of the MTJ with $t_{Bot\text{-}MgO} = 0.45$ nm and $t_{L5O} = 1.9$ nm, showing the maximum TMR ratio of 84 %. This relatively large TMR ratio is beyond the non-coherent tunneling case, as the TMR ratio is typically limited to be 10–30 % for MTJs with Fe electrodes and an amorphous alumina barrier [47]. This indicates that the L5O(001) barrier exhibits the TMR enhancement due to the coherent tunneling effect, similar to MgO(001) and MgAl$_2$O$_4$(001) barriers [8,48]. Furthermore, this indicates that the L5O(001) barrier has a band dispersion similar to that of MgO(001) [8] and various spinel oxides(001) [49,50], and exhibits high tunneling transmission through the evanescent Δ_1 Bloch state. The introduction of the ultrathin MgO insertions (less than a few monolayers) significantly improved the TMR ratio, suggesting that the interfacial structures at the Fe interfaces were improved due to suppression of interdiffusions and under/over oxidation. Such improvements have also been observed in MgGa$_2$O$_4$ barrier MTJs [19]. Therefore, further development of nano-insertion layers and composition control of the HEO layer are expected to improve the TMR ratio and interface PMA energy. Note that the linear increase in ln(RA) is observed over a wide range of $t_{Bot\text{-}MgO}$, indicating that the MgO/L5O/MgO functions as a single barrier layer.

Fig. 10d shows the current–voltage (IV) curve for the P state of the MTJ with $t_{Bot\text{-}MgO} = 0.3$ nm and $t_{L5O} = 1.75$ nm at RT. The positive bias voltage is defined as the direction in which electrons tunnel from the bottom electrode to the top electrode, as shown in the inset of Fig. 10d. Strong non-linearity at high bias is observed in the IV curve, indicating that the barrier height of L5O is much lower than that of an MgO barrier. The resistance is significantly reduced by bias application; a 1.5 V application results in ~ 1/30 of the zero bias value as shown in Supplementary S5 and Fig. S5. This feature will be effective for STT switching, which requires high current density, since significant current density acceleration can be obtained at high bias. We fit the curve using the Simmons model for the MTJ with $t_{Bot\text{-}MgO} = 0.45$ nm and $t_{L5O} = 1.9$ nm at RT [51], as shown in Supplementary S6 and Fig. S6, and obtain the effective barrier height φ_{eff} of 0.85 eV for the negative bias and 0.95 eV for the positive bias, about half or less of that of conventional MgO and

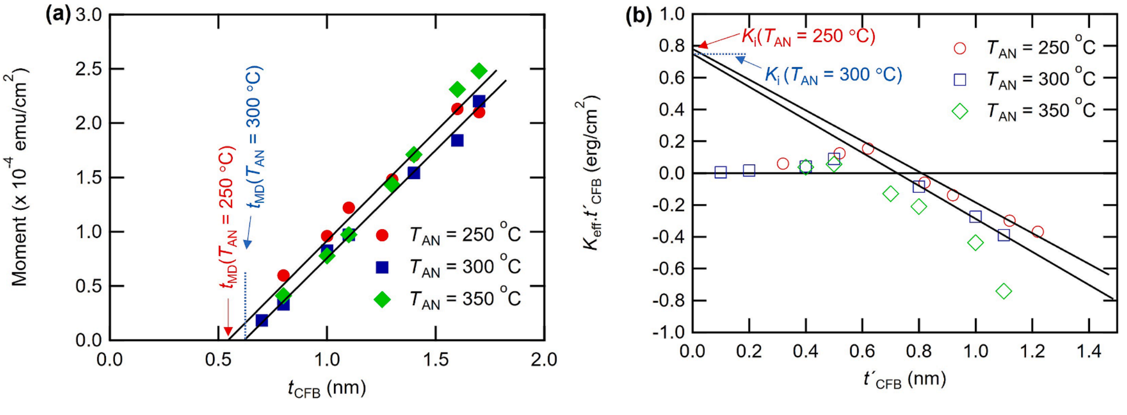

Fig. 9. Analysis of magnetic properties of L5O/CFB stacks. (a) Magnetic moment per unit area as a function of t_{CFB} of L5O/CFB (t_{CFB}) stacks after $T_{AN} = 250$ °C, 300 °C and 350 °C. Solid lines are the linear fit results. (b) Product of K_{eff} and effective CFB thickness t' as a function of t'. Solid lines are the linear fit results for the data range between $t' = 0.5$ nm and 1.2 nm for $T_{AN} = 250$ °C, and 300 °C.

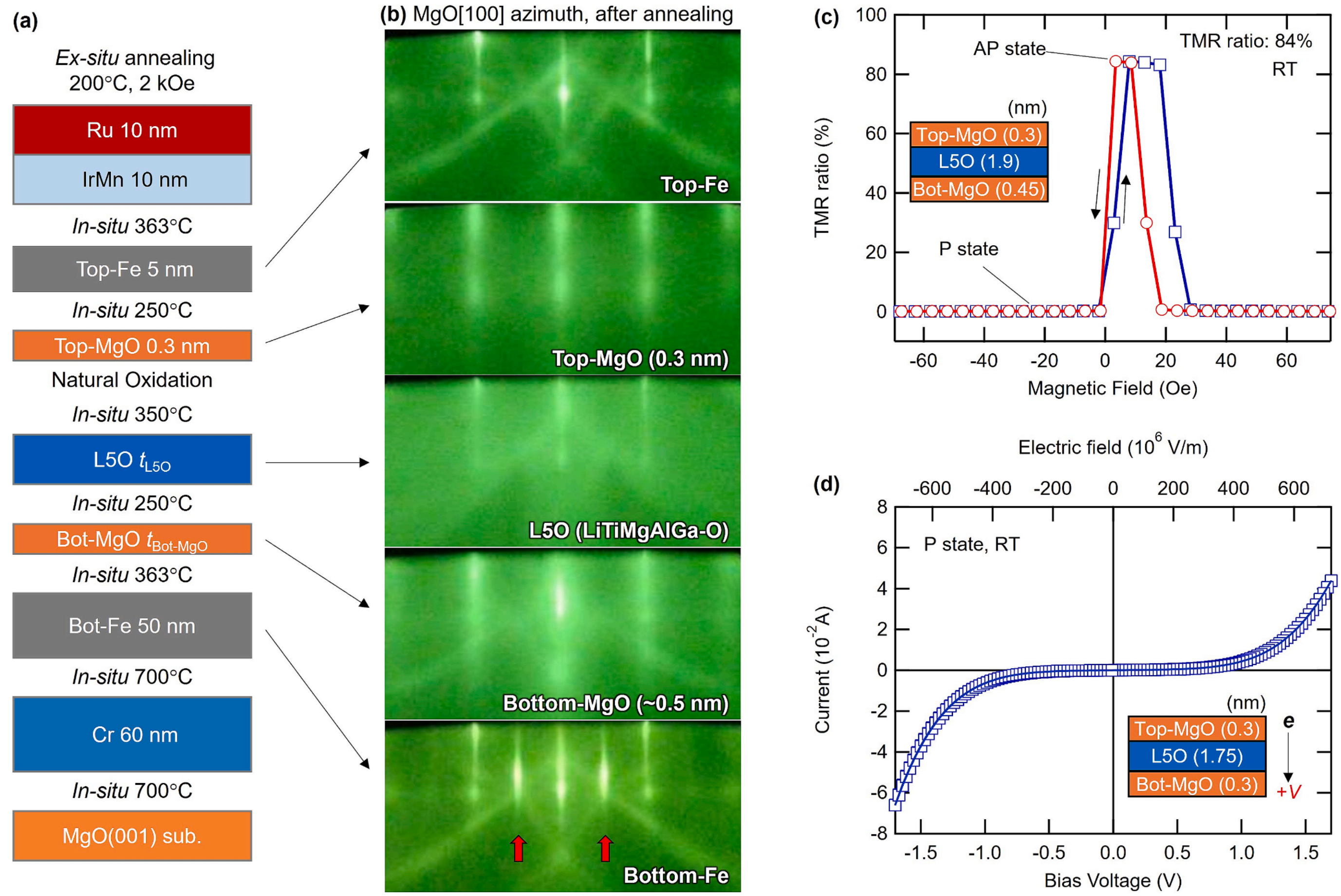

Fig. 10. Epitaxial growth and TMR properties of L5O-based barrier MTJs. (a) Schematic illustration of MTJ stacks. (b) RHEED patterns at each deposition stage (after post-annealing) for MgO[100] azimuth. (c) TMR ratio as a function of magnetic field of an Fe/MgO (0.45 nm)/L5O (1.9 nm)/MgO (0.3 nm)/Fe MTJ at RT. (d) *IV* curve for P state of Fe/MgO (0.3 nm)/L5O (1.75 nm)/MgO (0.3 nm)/Fe MTJ at RT.

$MgAl_2O_4$. The low barrier height of L5O suggests the possibility of a bandgap narrowing due to multivalent cations. Such an effect has been reported in the HEO spinel oxide $(Fe_{0.2}Co_{0.2}Ni_{0.2}Cu_{0.2}Zn_{0.2})Al_2O_4$, where the bandgap is narrower than the bandgaps of any of the parent spinel oxides [52]. Reducing the barrier height is essential for future MTJ applications, as a significant reduction in the *RA* value while maintaining the barrier thickness is required for read heads of HDDs and memory cells of MRAMs. We also find high DC breakdown voltages of 1.7–1.9 V for 2.3–2.4 nm total barrier thickness (corresponding breakdown electric fields of ~ 7.2–8.4×10^8 V/m) as shown in Supplementary S7 and Fig. S7, indicating that the structural stability of the barrier. These excellent properties of the L5O-based barrier indicate that a wide range of HEO materials are promising as MTJ barriers. For example, it can solve the problem of limited room for composition tuning for materials with a low barrier height, such as a ternary $MgGa_2O_4$ [19,53]. In addition, HEO ultrathin films can provide MTJ barriers with high structural stability due to the contribution of high entropy terms.

In order to highly design the compositions of HEO barriers, it is necessary to develop advanced theoretical methods for HEOs. MTJs and interface PMA structures always contain interfaces with magnetic layers, making it difficult to predict the optimal composition using conventional computational methods. Therefore, it will be necessary employ an alternative approach, such as a combination of quantum annealing, machine learning, and first-principles calculations [54].

Conclusions

In this study, we developed HEO thin films with a LiTiMgAlGaO composition, termed L5O, to explore their viability for spintronic device applications. By sputtering alternative layers of LTO and MAGO at atomic scale thicknesses of 0.3–0.5 nm on a single-crystal MgO(001) substrate, we achieved highly (001)-oriented epitaxial growth. The L5O film exhibits a rock-salt-like cation-disordered spinel structure, homogeneous cation distributions, and atomically flat surfaces. The lattice spacing of L5O is closely matched to the MgO substrate, confirming good heterostructure compatibility with typical FM materials used in MTJs while maintaining epitaxial relationships. Ultra-thin ($\sim$1 nm) CFB layers deposited on the L5O layer demonstrated pronounced perpendicular magnetization after post-annealing due to the large interface PMA energies reaching ~ 0.8 erg/cm^2 at the L5O/CFB interfaces. In addition, a TMR ratio of up to 84 % at RT was observed in Fe/MgO/L5O/MgO/Fe (001) MTJs, demonstrating the coherent tunneling mechanism through the HEO barrier. We also found that the significantly low barrier heights less than 1 eV, half or less of a conventional MgO barrier. This study highlights the excellent lattice matching with FMs, high structural stability, atomically flat interface, and the resultant substantial interface PMA, TMR enhancement by the coherent tunneling, and a significantly low barrier height, underscoring the significant potential of the HEOs for MTJ applications, including ultra-high-density MRAMs and MTJ-based AI devices. To further elucidate the functionalities of HEO systems with interfaces, development of advanced first-principles calculations that can deal with atomic disorder, vacancies, and interfaces with other materials will be critical to provide a deeper understanding of HEO based nano-electric and spintronic devices.

CRediT authorship contribution statement

Rombang Rizky Sihombing: Writing – review & editing, Writing – original draft, Visualization, Methodology, Investigation, Formal analysis, Data curation. **Thomas Scheike:** Writing – review & editing, Supervision, Methodology, Investigation. **Jun Uzuhashi:** Writing – review & editing, Visualization, Validation, Investigation, Formal analysis, Data curation, Conceptualization. **Hideyuki Yasufuku:** Data curation, Methodology, Software, Validation, Visualization, Writing – review & editing. **Tadakatsu Ohkubo:** Writing – review & editing, Visualization, Funding acquisition, Formal analysis, Data curation. **Zhenchao Wen:** Writing – review & editing, Methodology, Formal analysis, Data curation. **Seiji Mitani:** Writing – review & editing, Validation, Supervision, Methodology, Funding acquisition, Conceptualization. **Hiroaki Sukegawa:** Writing – review & editing, Writing – original draft, Visualization, Validation, Supervision, Methodology, Funding acquisition, Conceptualization.

Declaration of competing interest

The authors declare that they have no known competing financial interests or personal relationships that could have appeared to influence the work reported in this paper.

Acknowledgments

The authors thank Takanobu Hiroto for helping with the thin-film XRD experiments, Hiromi Ikeda and Chika Shigaki for their technical support on device microfabrication, and Kyoko Suzuki for her technical support on TEM observation. A part of this work was supported by the Electron Microscopy Unit, National Institute for Materials Science (NIMS). The part of XPS for this work was supported by "Advanced Research Infrastructure for Materials and Nanotechnology in Japan (ARIM)" of the Ministry of Education, Culture, Sports, Science and Technology (MEXT). Proposal Numbers JPMXP1224NM5242 and JPMXP1224NM5512. MEXT Program: Data Creation and Utilization-Type Material Research and Development Project (Grant No. JPMXP1122715503), MEXT Initiative to Establish Next-generation Novel Integrated Circuits Centers (X-NICS) (Grant No. JPJ011438), and JSPS KAKENHI (Grant Nos. 22H04966, and 24H00408). R.R.S. acknowledges NIMS for the provision of a NIMS Junior Research Assistantship.

Appendix A. Supplementary material

Supplementary data to this article can be found online at https://doi.org/10.1016/j.mattod.2025.06.025.

Data availability

Data will be made available on request.

References

[1] B. Cantor, et al., Microstructural development in equiatomic multicomponent alloys, Mater. Sci. Eng. A 375–377 (2004) 213–218, https://doi.org/10.1016/j.msea.2003.10.257.

[2] M.-H. Tsai, J.-W. Yeh, High-Entropy Alloys: a critical Review, Mater. Res. Lett. 2 (2014) 107–123, https://doi.org/10.1080/21663831.2014.912690.

[3] C.M. Rost, et al., Entropy-stabilized oxides, Nat. Commun. 6 (2015) 8485, https://doi.org/10.1038/ncomms9485.

[4] A. Sarkar, et al., High-Entropy Oxides: Fundamental Aspects and Electrochemical Properties, Adv. Mater. 31 (2019) 1806236, https://doi.org/10.1002/adma.201806236.

[5] G.N. Kotsonis, S.S.I. Almishal, F. Marques dos Santos Vieira, V.H. Crespi, I. Dabo, C. M. Rost, J.-P. Maria, High-entropy oxides: Harnessing crystalline disorder for emergent functionality, J. Am. Ceram. Soc. 106 (2023) 5587–5611. DOI: 10.1111/jace.19252.

[6] Y. Jiao, et al., Overview of high-entropy oxide ceramics, Mater. Today 77 (2024) 92–117, https://doi.org/10.1016/j.mattod.2024.06.005.

[7] H.J.M. Swagten, Chapter One Spin-Dependent Tunneling in Magnetic Junctions, in: Handb. Magn. Mater., Elsevier, 2007: pp. 1–121. DOI: 10.1016/S1567-2719(07)17001-3.

[8] W. Butler, et al., Spin-dependent tunneling conductance of Fe|MgO|Fe sandwiches, Phys. Rev. B 63 (2001) 054416, https://doi.org/10.1103/PhysRevB.63.054416.

[9] J. Mathon, A. Umerski, Theory of tunneling magnetoresistance of an epitaxial Fe/MgO/Fe(001) junction, Phys. Rev. B 63 (2001), https://doi.org/10.1103/PhysRevB.63.220403, 220403(R).

[10] H. Sukegawa, et al., Enhanced tunnel magnetoresistance in a spinel oxide barrier with cation-site disorder, Phys. Rev. B 86 (2012) 184401, https://doi.org/10.1103/PhysRevB.86.184401.

[11] S. Ikeda, et al., A perpendicular-anisotropy CoFeB–MgO magnetic tunnel junction, Nat. Mater. 9 (2010) 721–724, https://doi.org/10.1038/nmat2804.

[12] J.W. Koo, et al., Large perpendicular magnetic anisotropy at Fe/MgO interface, Appl. Phys. Lett. 103 (2013) 192401, https://doi.org/10.1063/1.4828658.

[13] J. Okabayashi, et al., Perpendicular magnetic anisotropy at the interface between ultrathin Fe film and MgO studied by angular-dependent x-ray magnetic circular dichroism, Appl. Phys. Lett. 105 (2014) 122408, https://doi.org/10.1063/1.4896290.

[14] S.S.P. Parkin, et al., Giant tunnelling magnetoresistance at room temperature with MgO (100) tunnel barriers, Nat. Mater. 3 (2004) 862–867, https://doi.org/10.1038/nmat1256.

[15] S. Yuasa, et al., Giant room-temperature magnetoresistance in single-crystal Fe/MgO/Fe magnetic tunnel junctions, Nat. Mater. 3 (2004) 868–871, https://doi.org/10.1038/nmat1257.

[16] S. Bhatti, et al., Spintronics based random access memory: a review, Mater. Today 20 (2017) 530–548, https://doi.org/10.1016/j.mattod.2017.07.007.

[17] G. Albuquerque, et al., HDD Reader Technology Roadmap to an Areal Density of 4 Tbpsi and beyond, IEEE Trans. Magn. 58 (2022) 3100410, https://doi.org/10.1109/TMAG.2021.3081042.

[18] H. Sukegawa, et al., $MgGa_2O_4$ spinel barrier for magnetic tunnel junctions: Coherent tunneling and low barrier height, Appl. Phys. Lett. 110 (2017) 122404, https://doi.org/10.1063/1.4977946.

[19] R.R. Sihombing, et al., Enhanced tunnel magnetoresistance of $Fe/MgGa_2O_4/Fe$ (001) magnetic tunnel junctions by interface-tuning with atomic-scale MgO insertion layers, Appl. Phys. Lett. 126 (2025) 022407, https://doi.org/10.1063/5.0247660.

[20] R. Shan, et al., Demonstration of Half-Metallicity in Fermi-Level-Tuned Heusler Alloy $Co_2FeAl_{0.5}Si_{0.5}$ at Room Temperature, Phys. Rev. Lett. 102 (2009) 246601, https://doi.org/10.1103/PhysRevLett.102.246601.

[21] H. Sukegawa, et al., Tunnel magnetoresistance with improved bias voltage dependence in lattice-matched Fe/spinel $MgAl_2O_4$/Fe(001) junctions, Appl. Phys. Lett. 96 (2010) 212505, https://doi.org/10.1063/1.3441409.

[22] T. Scheike, H. Sukegawa, S. Mitani, Li-substituted $MgAl_2O_4$ barriers for spin-dependent coherent tunneling, Jpn. J. Appl. Phys. 55 (2016) 110310, https://doi.org/10.7567/JJAP.55.110310.

[23] Ikhtiar, et al., Magnetic tunnel junctions with a rock-salt-type $Mg_{1-x}Ti_xO$ barrier for low resistance area product, Appl. Phys. Lett. 108 (2016) 242416, https://doi.org/10.1063/1.4953783.

[24] T. Scheike, et al., Exceeding 400% tunnel magnetoresistance at room temperature in epitaxial Fe/MgO/Fe(001) spin-valve-type magnetic tunnel junctions, Appl. Phys. Lett. 118 (2021) 042411, https://doi.org/10.1063/5.0037972.

[25] J. Uzuhashi, et al., Experimental investigation and simulation of SEM image intensity behaviors for developing thickness-controlled S/TEM lamella preparation via FIB-SEM, Microscopy (2025) dfaf006, https://doi.org/10.1093/jmicro/dfaf006.

[26] H. Sukegawa, et al., Enhanced tunnel magnetoresistance in a spinel oxide barrier with cation-site disorder, Phys. Rev. B 86 (2012) 184401, https://doi.org/10.1103/PhysRevB.86.184401.

[27] J.P. Hadorn, et al., Microstructural evolution of perpendicular magnetization films with an ultra-thin $Co_2FeAl/MgAl_2O_4$(001) structure, Acta Mater. 145 (2018) 306–315, https://doi.org/10.1016/j.actamat.2017.12.018.

[28] M. Belmoubarik, et al., $MgAl_2O_4$(001) based magnetic tunnel junctions made by direct sputtering of a sintered spinel target, Appl. Phys. Lett. 108 (2016) 132404, https://doi.org/10.1063/1.4945049.

[29] A.Y. Lee, et al., Development of the NIST X-ray Photoelectron Spectroscopy (XPS) Database, Version 5, Data Sci. J. 23 (2024) 45, https://doi.org/10.5334/dsj-2024-045.

[30] F. Khairallah, A. Glisenti, XPS Study of MgO Nanopowders Obtained by Different Preparation Procedures, Surf. Sci. Spectra 13 (2007) 58–71, https://doi.org/10.1116/11.20060601.

[31] P. Delichere, S. Daniele, L.G. Hubert-Pfalzgraf, Surface Segregation Study of Transparent $ZnGa_2O_4$ Films by XPS, Surf. Sci. Spectra 8 (2003) 303–311, https://doi.org/10.1116/11.20020501.

[32] I. Olefjord, H.J. Mathieu, P. Marcus, Intercomparison of surface analysis of thin aluminium oxide films, Surf. Interface Anal. 15 (1990) 681–692, https://doi.org/10.1002/sia.740151108.

[33] H. Idriss, On the wrong assignment of the XPS O1s signal at 531–532 eV attributed to oxygen vacancies in photo- and electro-catalysts for water splitting and other materials applications, Surf. Sci. 712 (2021) 121894, https://doi.org/10.1016/j.susc.2021.121894.

[34] C. Sleigh, et al., On the determination of atomic charge via ESCA including application to organometallics, J. Electron Spectrosc. Relat. Phenom. 77 (1996) 41–57, https://doi.org/10.1016/0368-2048(95)02392-5.

[35] D. Gonbeau, et al., XPS study of thin films of titanium oxysulfides, Surf. Sci. 254 (1991) 81–89, https://doi.org/10.1016/0039-6028(91)90640-E.

[36] S. Tanaka, M. Taniguchi, H. Tanigawa, XPS and UPS studies on electronic structure of Li_2O, J. Nucl. Mater. 283–287 (2000) 1405–1408, https://doi.org/10.1016/S0022-3115(00)00251-8.

[37] Q. Xiang, et al., Large perpendicular magnetic anisotropy in epitaxial Fe/$MgAl_2O_4$(001) heterostructures, Appl. Phys Express 11 (2018) 063008, https://doi.org/10.7567/APEX.11.063008.

[38] S. Kobayashi, et al., Perpendicular magnetic Anisotropy of an Ultrathin Fe Layer Grown on NiO(001), Phys. Rev. Appl. 19 (2023) 064005, https://doi.org/10.1103/PhysRevApplied.19.064005.

[39] W.C. Tsai, et al., Investigation of perpendicular magnetic anisotropy of CoFeB by x-ray magnetic circular dichroism, Appl. Phys. Lett. 100 (2012) 172414, https://doi.org/10.1063/1.4707380.

[40] J. Sinha, et al., Enhanced interface perpendicular magnetic anisotropy in Ta|CoFeB|MgO using nitrogen doped Ta underlayers, Appl. Phys. Lett. 102 (2013) 242405, https://doi.org/10.1063/1.4811269.

[41] S. Ikeda, et al., Boron Composition Dependence of magnetic Anisotropy and Tunnel Magnetoresistance in MgO/CoFe(B) based Stack Structures, IEEE Trans. Magn. 48 (2012) 3829–3832, https://doi.org/10.1109/TMAG.2012.2203588.

[42] D.C. Worledge, et al., Spin torque switching of perpendicular Ta|CoFeB|MgO-based magnetic tunnel junctions, Appl. Phys. Lett. 98 (2011) 022501, https://doi.org/10.1063/1.3536482.

[43] Z. Wen, et al., A 4-Fold-Symmetry Hexagonal Ruthenium for magnetic Heterostructures Exhibiting Enhanced Perpendicular magnetic Anisotropy and Tunnel Magnetoresistance, Adv. Mater. 26 (2014) 6483–6490, https://doi.org/10.1002/adma.201401959.

[44] Y. Liu, L. Hao, J. Cao, Effect of annealing conditions on the perpendicular magnetic anisotropy of Ta/CoFeB/MgO multilayers, AIP Adv. 6 (2016) 045008, https://doi.org/10.1063/1.4947132.

[45] C. Chappert, P. Bruno, Magnetic anisotropy in metallic ultrathin films and related experiments on cobalt films (invited), J. Appl. Phys. 64 (1988) 5736–5741, https://doi.org/10.1063/1.342243.

[46] H. Sukegawa, et al., Perpendicular magnetic anisotropy at lattice-matched $Co_2FeAl/MgAl_2O_4$(001) epitaxial interfaces, Appl. Phys. Lett. 110 (2017) 112403, https://doi.org/10.1063/1.4978663.

[47] S. Yuasa, et al., Magnetic tunnel junctions with single-crystal electrodes: a crystal anisotropy of tunnel magneto-resistance, Europhys. Lett. 52 (2000) 344, https://doi.org/10.1209/epl/i2000-00445-5.

[48] M. Coll, et al., Towards Oxide Electronics: a Roadmap, Appl. Surf. Sci. 482 (2019) 1–93, https://doi.org/10.1016/j.apsusc.2019.03.312.

[49] Y. Miura, et al., First-principles study of tunneling magnetoresistance in Fe/$MgAl_2O_4$/Fe(001) magnetic tunnel junctions, Phys. Rev. B 86 (2012) 024426, https://doi.org/10.1103/PhysRevB.86.024426.

[50] J. Zhang, X.-G. Zhang, X.F. Han, Spinel oxides: Δ_1 spin-filter barrier for a class of magnetic tunnel junctions, Appl. Phys. Lett. 100 (2012) 222401, https://doi.org/10.1063/1.4722804.

[51] J.G. Simmons, Generalized Formula for the Electric Tunnel effect between Similar Electrodes Separated by a Thin Insulating Film, J. Appl. Phys. 34 (1963) 1793–1803, https://doi.org/10.1063/1.1702682.

[52] R.R. Katzbaer, et al., Band Gap Narrowing in a High-Entropy Spinel Oxide Semiconductor for Enhanced Oxygen Evolution Catalysis, J. Am. Chem. Soc. 145 (2023) 6753–6761, https://doi.org/10.1021/jacs.2c12887.

[53] S. Mertens, et al., MgGa $_2$ O $_4$ as alternative barrier for perpendicular MRAM junctions and VCMA, Appl. Phys. Lett. 118 (2021) 172402, https://doi.org/10.1063/5.0046554.

[54] K. Nawa, et al., Quantum Annealing Optimization Method for the Design of Barrier Materials in magnetic Tunnel Junctions, Phys. Rev. Appl. 20 (2023) 024044, https://doi.org/10.1103/PhysRevApplied.20.024044.